Materials Advances

ROYAL SOCIETY OF CHEMISTRY

PAPER

View Article Online
View Journal | View Issue

Check for updates

Cite this: *Mater. Adv.*, 2025, **6**, 319

Received 11th September 2024,
Accepted 20th November 2024

DOI: 10.1039/d4ma00921e

rsc.li/materials-advances

Nanocrystalline and mesoporous (Ba,Sr)(Sn,Mn)O_3 perovskite solid solution: a potential n-type semiconductor for room temperature ethanol sensing applications†

Nehal Ashok Waghchoure and Kampurath Poduvattil Jayadevan *

In this study, we report a potential n-type semiconducting nanocrystalline perovskite solid solution that is represented as (Ba,Sr)(Sn,Mn)O_3 with a specific composition of $Ba_{0.98}Sr_{0.02}Sn_{0.95}Mn_{0.05}O_3$ for room temperature (∼25 °C) chemo-resistive ethanol sensing application. The perovskite solid solution has been prepared using a co-precipitation route and calcined at 700 °C. XRD and SAED confirm the perovskite formation. The process of crystallisation has been confirmed through thermal analysis. FESEM analysis reveals a cubic morphology and EDS-based elemental mapping confirms the presence of all elements in their approximate ratio. Ethanol sensing shows a relatively fast sensor response (∼1.06 s) and recovery (∼1.81 s) time at room temperature and ∼55% humidity. The stable sensor response is attributed to the improvement in BET-specific surface area (∼5 $m^2\ g^{-1}$), narrow slit mesopores (3.2 nm), and the core level shifts in the binding energy of O 1s as revealed by X-ray photoelectron spectroscopy (XPS). These are indicative of conducive surface-active sites for ethanol sensing. The positive slope of the Mott–Schottky plot indicates the n-type semiconducting behaviour of the synthesized perovskite solid solution.

1. Introduction

Lead (Pb)-free oxide perovskites, alkaline earth stannate perovskites ($MSnO_3$ where M = Ba, Sr) and their solid solutions have been investigated recently for their use as transparent conducting oxide (TCO) electrodes in electronic devices[1] and electrical devices[2,3] and for their optical properties,[4,5] catalysis,[6,7] photovoltaics,[8–10] optoelectronics,[11] and spintronics.[12,13] The use of perovskites as sensors to sense volatile organic compounds (VOCs) is well-known.[14] The efficacy of oxide perovskites as VOC gas sensors is greatly influenced by their crystal structure. Perovskites' distinct structural characteristics affect their surface, optical, and electrical properties, which are vital for gas-sensing applications. Oxide perovskites have a general formula ABO_3. Selecting A and B gives the freedom to adjust the surface and electrical characteristics, which can improve their interaction with VOC molecules. Additionally, compositional changes and synthesis techniques may alter perovskites' surface area and porosity.[15] The structure's capacity to accommodate a broad range of metal cations on both A and B sites makes the ABO_3 perovskite oxide family a genuine gold mine of varied physical characteristics.[16,17] The rotations of the BO_6 octahedral network (also known as octahedral tilt) are used to accommodate the A cation when its size is less than that needed for an ideal cubic unit cell.[18] These changes alter the B–O bond length and B–O–B bond angles, thereby changing the electronic and magnetic properties of the materials. These unique features make perovskites the most challenging and effective materials for VOC sensing.[19,20] Perovskites are also known for their oxygen vacancy-induced properties. The oxygen vacancy-induced defective $ABO_{3-\delta}$ structure is thermodynamically more favourable.[21] The scope of formation of defects, porosity, and ease of adsorption of gaseous species on the doped oxide perovskite surfaces would make this class of compounds suitable for real-time sensor applications at room temperature.[22]

The emerging applications of oxide perovskites have led to a flurry of research activities on $BaSnO_3$ (BSO) and its doped variants.[14] VOCs vaporise readily as they have high vapour and atmospheric pressure at room temperature. VOCs may emanate naturally or through human activities.[23] Due to the rapid growth in urbanisation and industrialisation, using VOCs in industries and releasing those into the atmosphere has become a matter of concern.[24–26] Exposure to a high concentration of these compounds for a long period may cause a lot of health issues and sometimes may be lethal. Therefore, their detection at the early stage is of utmost importance.[27,28] A gas sensor is

---

Energy and Environmental Chemistry Laboratory, Department of Chemistry Birla Institute of Technology and Science, NH17B, Zuarinagar, Vasco da Gama, 403726, India. E-mail: jayadev@goa.bits-pilani.ac.in

† Electronic supplementary information (ESI) available. See DOI: **https://doi.org/10.1039/d4ma00921e**

one of the finest devices made by human intelligence to sense the gas and raise the alarm if the concentration is lethal for humans.[29–31] Among the VOCs, ethanol is the most commonly used raw material in industries for synthesising organic molecules.[32,33] Ethanol, however, ignites when exposed to high temperatures or close to open flames. Furthermore, when it comes into contact with oxidants, it becomes vulnerable to chemical reactions or combustion.[34,35] As per the reports from the World Health Organization (WHO), more than 3 million people lose their lives annually due to the health issues caused by ethanol and its consumption *via* liquor.[36] Ethanol is also a volatile substance. A significant concentration of ethanol vapour in the atmosphere can harm the human neurological and circulatory systems, impairing eyesight and the respiratory tract's mucous membrane.[37] Gas sensors may be divided into several categories based on how they work, including solid electrolyte gas sensors, thermal conductivity gas sensors, semiconductor gas sensors (also known as chemo-resistive gas sensors), and catalytic combustible gas sensors.[38] In a ravishing array of multiple sensors, chemo-resistive gas sensors based on heterojunctions made from metal oxide/metal oxide, metal oxide/noble metal, metal oxide/metal sulphide, and metal oxide/other materials have been studied for numerous applications in tracking food safety, air quality, and leakage of toxic gases (*i.e.*, NO_x, CO) and volatile organic compounds (acetone, ethanol, ammonia, *etc.*). The receptor (recognition) function, transducer function, and peculiarities of sensor architecture are three separate elements that govern the operating properties of chemo-resistive gas sensors, particularly sensitivity. The receptor function provides the oxide surface's capacity to interact with the target gas. The transducer function can transform the signal produced by the chemical interaction of the oxide surface into an electrical signal.[39] The development of ternary oxide and its heterostructures may bring a ray of hope by reducing the response and recovery time. Regarding cost and manufacturing procedures, chemo-resistive ethanol sensors are the best compared to fuel cell ethanol sensors.[40] Transition-metal oxides are more appropriate for gas sensing because they have many preferred oxidation states. Metal oxides adorned with noble metals and ternary, quaternary, or binary metals are typically utilised for sensitive detection at ppb levels.[41] In particular, doping stannate with a transition metal like manganese (Mn), which exhibits a range of oxidation states, has been a topic of intense research interest as the valence state fluctuations in Mn would lead to defects in the oxygen sublattice, thereby introducing intermediate electronic states in the bandgap.[42–44] Pèna and Fierro[45] in their detailed review of the performance of perovskite oxides have proposed total oxygen adsorption on the surface of perovskite oxides. As per their analysis, the presence of Mn in the perovskites results in high affinity towards adsorbed oxygen, thereby promoting the oxidation of ethanol.

The BSO phase and its crystal structure have been well studied, and it is known to be close to an ideal cubic perovskite with a tolerance factor of 0.93 and a lattice parameter of ∼4.11 Å with a space group of $Pm\bar{3}m$.[46] $SrSnO_3$ is orthorhombic with lattice parameters a = 5.74 Å, b = 8.10 Å, and c = 5.73 Å and the *Pbnm* space group.[47] Along with the tolerance factor, the octahedral factor (r_B/r_O) also plays a vital role in determining the stability of the ABO_3 perovskites.[48] BO_6 is the basic unit of perovskites, so the octahedral factor r_B/r_O related to the stability of octahedron BO_6 is another governing parameter for the formability of perovskites. Even though there is a lack of structural match in terms of symmetry, the feasibility of a solid solution has been predicted experimentally by Udawatte *et al.*[49] and computationally by Freitas *et al.*[50] A few studies have been reported on the effect of the substitution of Mn on the properties of BSO.[42] These reports indicate that the electronic energy band gap gets affected in the presence of Mn, and the resultant properties can be exploited for their potential applications, such as photocatalysis. The exceptional properties of Mn (like dielectric and magnetic properties) prompted us to investigate the nature of Mn-doped $Ba_{1-x}Sr_xSnO_3$ solid solution oxides. The tolerance factor calculated is estimated to be close to unity for this solid solution.[51] It was observed that doping Mn at the Sn site reduces the bandgap to a minimal extent from 3.23 eV to 3.01 eV in BSO.[52] But, doping Sr at the Ba site and Mn at Sn reduces the bandgap greatly due to the distortion caused by Sr after doping it at the Ba site, although in our sample, the distortion may be negligible because the % ratio of Ba : Sr is 98 : 2, retaining the cubic structure intact. As per research reports, the Sr at the 'A' site reduces the leaching of manganese doped at the 'B' site.[53] However, as far as our knowledge is concerned, the complex interplay of lattice distortion, strain, electronic states and resultant optical absorption characteristics of Mn-doped $(Ba,Sr)SnO_3$ has been rarely investigated; therefore, this research reveals the effect of both these elements (Sr and Mn) on the optical and structural properties and explores the sensor applications of this potential semiconducting oxide solid solution. In the present study to prepare the $(Ba,Sr)(Sn,Mn)O_3$ solid solution, we have adopted a surfactant-free co-precipitation method that would result in a cubic morphology through a process of 'dissolution–recrystallization' of the hydroxylated precursor of general formula $MSn(OH)_6$. The crystals undergo an Ostwald-ripening process, resulting in a cubic morphology for the $(Ba,Sr)(Sn,Mn)O_3$ solid solution.[54] The schematic figure showing the formation of cubic morphology for the solid solution is shown in Fig. S5 (ESI†).

2. Materials and methods

2.1 Chemical reagents

The precursor, namely, barium nitrate $[Ba(NO_3)_2]$ (98.5% pure), was brought from Loba Chemie, and stannic chloride $[SnCl_4]$ (98% pure) was purchased from Sigma-Aldrich and Merck Life Sciences. Manganese(II) nitrate tetrahydrate $[Mn(NO_3)_2 \cdot 4H_2O]$ (99.98%) and NaOH (A grade) were purchased from Sigma-Aldrich and Merck Life Science, respectively. Changshu Hongsherg Fine Chemicals supplied ethanol, while Sisco Research Laboratories provided isopropyl alcohol and acetone (for VOC analysis). The reagents were used without any further purification.

2.2 Preparation of $Ba_{0.98}Sr_{0.02}Sn_{0.95}Mn_{0.05}O_3$

The aqueous solutions of $Ba(NO_3)_2$ and $Sr(NO_3)_2$ were prepared by dissolving stoichiometric amounts of $Ba(NO_3)_2$ and $Sr(NO_3)_2$ together in 25 mL of distilled water. The aqueous solution of $SnCl_4$ and $Mn(NO_3)_2{\cdot}4H_2O$ was prepared by dissolving the stoichiometric amount of both precursors in 10 mL of distilled water. The aqueous solution of $SnCl_4$ and $Mn(NO_3)_2{\cdot}4H_2O$ was added dropwise to the above solution of $Ba(NO_3)_2$ and $Sr(NO_3)_2$ with vigorous stirring for 1 hour. Once the homogenous solution was formed, the aqueous solution of NaOH was added dropwise to the above homogenous solutions and stirred for almost 30 min. Subsequently, the whole solution was heated at 70 °C for 3 h and vigorously stirred until the precipitate formed. This formed precipitate was then dried at 80 °C for another 3 h in a Petri dish. The dried precipitate was ground using a mortar and pestle, then transferred to an alumina crucible and heated at 200 °C in a muffle furnace for 2 h. It was then washed with 15 mL of distilled water, dried at 80 °C for 30 mins and then again heated at 200 °C for 2 h. The washing step was introduced just to remove impurities like carbonates, nitrates, sodium, and chlorine ions from the product. This process was repeated thrice and then the product was heated at 500 °C for 2 h and later calcined at 700 °C for 2 h and cooled at room temperature. It was then ground and used for further analysis.

2.3 Characterization

The phase structure and microstructures were measured by X-ray diffraction (XRD) using a Bruker D8 Advance with Cu Kα radiation (λ = 1.542 Å) from 20° to 80° with a step size of 0.02° and a step time of 0.6 s. A Quanta FEG 250 was used for field emission scanning electron microscopy (FESEM) analysis and for performing energy dispersive spectroscopy (EDS) measurements. The accelerating voltage for the FESEM and EDS measurements was 20 kV each. A LEICA EM ACE 200 was used for gold sputtering. Raman spectra were recorded in the back-scattering configuration on a LAB RAM HR Horiba France by using a 532 nm Nd-YAG laser (3.2 mW) as a laser source. All these analyses were carried out at the CSIF lab (BITS Pilani, KK Birla Goa Campus). X-ray photoelectron spectroscopy (XPS) was carried out using an XPS system from Thermo Fischer Scientific, with Al Kα radiation at 1486.6 eV, at Central Analytical Laboratory (CAL), BITS-Pilani, Hyderabad. Transmission electron microscopy (TEM) analysis was carried out using a JEM-2100 PLUS (Central Facility Centre, Shivaji University Kolhapur) with a resolution of up to 0.19 nm. UV-vis absorption spectra were recorded using a Jasco V 550 spectrometer, Brunauer–Emmett–Teller (BET) analysis was carried out at a degassing temperature of 90 °C for 3 h on a Quantachrome Instrument, Model: 20e and higher, NovaWin Version: 11.01–11.0x (in-house facility), and thermogravimetric analysis (TGA) and differential scanning calorimetry (DSC) analysis were performed using a Shimadzu DSC-60 in normal air from Savitribai Phule Pune University (SPPU). The electrochemical study was performed using a BioLogic SP-150e electrochemical workstation. Using a three-electrode electrochemical cell for electrochemical impedance spectroscopy (EIS) and chronoamperometric data, the Mott–Schottky plot was created. The Mott–Schottky plots were produced using EIS measurements, which had a frequency range of 100 kHz to 10 Hz and an Ag/AgCl reference electrode between −1.1 V and −0.1 V. For the photocatalyst-working electrode, the BSO slurry was prepared in ethanol using alcoholic Nafion as a binder. Next, it was applied to a 1 cm^2 surface area on fluorine-doped tin oxide (FTO) glass slides. Graphite served as the counter electrode and an Ag/AgCl (saturated KCl) electrode as the reference electrode. The sensor application of the substrates was carried out in the Semiconductors Materials and Device Laboratory, Department of Physics, BITS Pilani, KK Birla Goa campus.

2.4 Fabrication and measurement of sensors

The ITO plate (1 cm^2) having a 1 mm thick trench over the surface was washed with Milli-Q water and then sonicated with ethanol, acetone, and Milli-Q water for 30 min each. The above-prepared $Ba_{0.98}Sr_{0.02}Sn_{0.95}Mn_{0.05}O_3$ was dropcast over a trench on a 1 cm^2 ITO plate. The sensor substrate was dried in an oven at 80 °C for 1 h before use. The electrical contacts were made by clamping the clips on both ends of the ITO plate. In the sensor chamber where the device is exposed to the testing gas, pure liquid is vaporized to achieve the necessary concentration of the test gas. All the sensing measurements were conducted at room temperature (∼25 °C). A schematic experimental setup for the VOC analysis is shown in Fig. S9a and the original experimental setup is shown in Fig. S9b (ESI†). The following formula was used to determine the concentration of the gaseous species in a known volume of liquid within the test chamber.[55,56]

$$v = \frac{C \times M \times V \times T}{22.4 \times \rho \times t \times P} \tag{1}$$

where v (μL) is the volume of the liquid, C (ppm) is the expected concentration of the liquid in the sensor chamber, M (g mol^{-1}) is the molecular weight of the liquid, V (L) is the volume of the sensor chamber, T (K) is the room temperature (∼25 °C), 22.4 is the molar volume of the gas (L mol^{-1}) at Standard Temperature and Pressure (STP), ρ (g mL^{-1}) is the density of the volatile compound under study, t (K) is the temperature inside the sensor chamber, and P is the purity of the liquid. By examining the variations in electrical resistance following gas exposure, the device's sensing capability was assessed. The Keithley Source Measurement Unit (SMU-2450) with a bias voltage of 5 V was used to measure the variations in resistance. R_a/R_g, where R_a is the resistance in air and R_g is the resistance under the target gas, is the definition of the sensor response (S) of the apparatus. The resistance's rise from zero to 90% of its maximum level is measured by the response time (T_r), and its fall from 90% to 10% of its maximum level is measured by the recovery time (T_{rc}).[57] The T_r was calculated when the sensor substrate was exposed to ethanol gas of specific concentration for 40 seconds (s) in the sensor chamber, and the T_{rc} was calculated when the substrate was exposed to the ambient environment for 10 seconds (s) outside the sensor chamber.

3. Results and discussion

3.1 XRD analysis

The peaks at 30.67°, 43.95°, 54.53°, 63.89°, and 72.56° are attributed to the 110, 200, 211, 210, and 310 planes, respectively. In Fig. 1a, the highest intense peak is observed at 30.6°. The highly intense peak depicts the crystalline nature of the synthesised $Ba_{0.98}Sr_{0.02}Sn_{0.95}Mn_{0.05}O_3$. It was observed that doping Sr and Mn hardly altered the XRD spectra, indicating that it has minimal impact on the crystal lattice structure of $BaSnO_3$ (4.116 Å). However, it is possible to obtain trace amounts of respective binary oxides of Sn and Mn with an increasing amount of Mn being added to the perovskite structure. The XRD peaks of the Mn-doped $Ba_{0.98}Sr_{0.02}SnO_3$ consisting of different concentrations of Mn are also studied, the details of which are provided in the ESI.† The crystallite size was calculated using Scherrer's equation

$$D = \frac{K\lambda}{\beta \cos\theta} \tag{2}$$

where D is the crystallite size, K is the shape factor (0.9), λ is the wavelength, β is the full width at half maxima (FWHM), and θ is the diffraction angle. The crystallite size of $Ba_{0.98}Sr_{0.02}Sn_{0.95}Mn_{0.05}O_3$ is 28.26 nm. It is observed that as the Mn concentration increases, there is a decrease in the crystallite size. The ionic size of Mn^{4+} is 53 pm and that of Sn^{4+} is 69 pm, which is why the crystallite size decreases with the increase in the concentration of Mn, which substitutes Sn to some extent in the perovskites.[58] It is confirmed that the dopant Mn ion plays a vital role in the growth mechanism of the synthesised compound by widening the peak, followed by a drop in crystallite size with an increase in the Mn concentration. The lattice constant of $Ba_{0.98}Sr_{0.02}Sn_{0.95}Mn_{0.05}O_3$ is 4.112 Å. The reduction in the lattice constant (a) for the above sample indicates the presence of oxygen vacancies.[59] Fig. S1a (ESI†) shows the XRD plots for Mn-doped/undoped $Ba_{0.98}Sr_{0.02}SnO_3$ perovskites. Fig. S1b (ESI†) shows the Rietveld refinement plot of $Ba_{0.98}Sr_{0.02}Sn_{0.95}Mn_{0.05}O_3$, which was obtained using Profex 5.2 software, and the details are provided in the ESI.† It was found that as the crystallite size decreases, the micro-strain increases. The crystallite size that is estimated using Willamson–Hall (W–H) analysis is ~42 nm for $Ba_{0.98}Sr_{0.02}Sn_{0.95}Mn_{0.05}O_3$ (Fig. 1b) and for other compositions, the details are provided in the ESI† (Fig. S2). The strain in the above sample was calculated *via* a W–H plot and was $\sim 2.04 \times 10^{-3}$. The thermogravimetric analysis of the samples was carried out and a weight loss of 15% was observed for the decomposition of the hydroxyl precursors to the final product.[60] The details of the TGA/DSC analysis are provided in the ESI† (Fig. S6).

3.2 Morphological analysis

The FE-SEM image of $Ba_{0.98}Sr_{0.02}Sn_{0.95}Mn_{0.05}O_3$ is shown in Fig. 2. Fig. 2a displays the perfect cubic morphology of $Ba_{0.98}Sr_{0.02}Sn_{0.95}Mn_{0.05}O_3$. It can be seen that the cubes are compactly packed and well segregated from each other. The $Ba_{0.98}Sr_{0.02}Sn_{0.95}Mn_{0.05}O_3$ cubes have a rough surface and show the settlement of some particles, which may be of hydroxylated cations over the surface.[60] The dopant atoms (Sr and Mn) are well diffused into the lattice and induce a considerable variation in the cubic size. The EDS analysis of the doped samples confirms the presence of Sr and Mn in the Ba–Sn–O lattice. The weight % and atomic % of elements of $Ba_{0.98}Sr_{0.02}Sn_{0.95}Mn_{0.05}O_3$ are shown in Fig. S3 (ESI†). The elemental mapping of $Ba_{0.98}Sr_{0.02}Sn_{0.95}Mn_{0.05}O_3$ was also carried out and it shows the presence of all the elements uniformly spread across the cube (Fig. 3). The FESEM images of the other Mn-doped/undoped $Ba_{0.98}Sr_{0.02}SnO_3$ also showed the cubic morphology having a rough surface (Fig. S4, ESI†).

Fig. 2b shows the TEM image of $Ba_{0.98}Sr_{0.02}Sn_{0.95}Mn_{0.05}O_3$ having cubic morphology. The size of the cube is estimated to be ~0.6 μm. The HRTEM image (Fig. 2c) for $Ba_{0.98}Sr_{0.02}Sn_{0.95}Mn_{0.05}O_3$ shows an inter-planar spacing of 0.29 nm, which is attributed to the lattice plane of (110). Fig. 2d shows the SAED image of $Ba_{0.98}Sr_{0.02}Sn_{0.95}Mn_{0.05}O_3$. The XRD measurements of these samples indicated that they are crystalline, and the

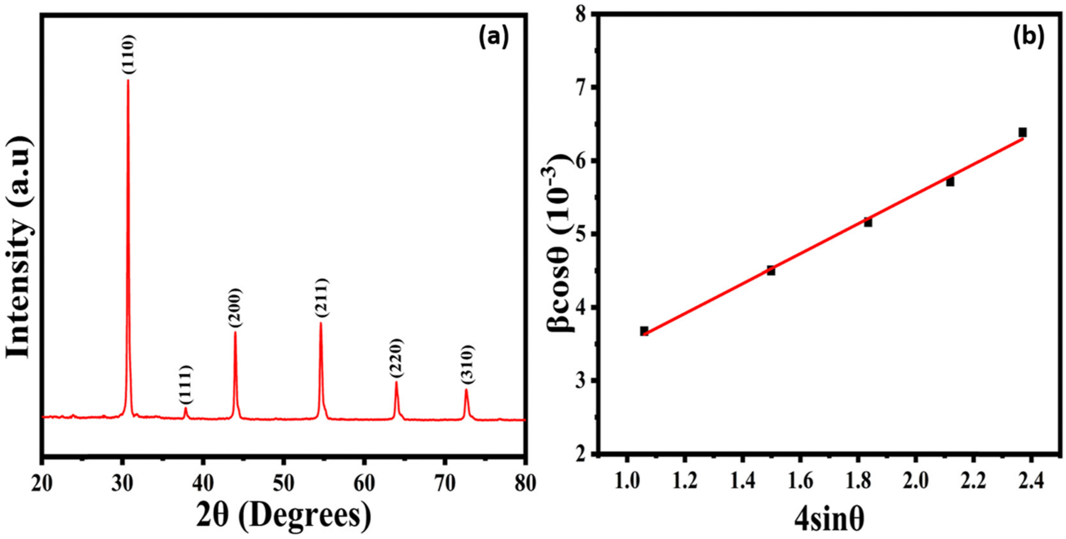

Fig. 1 (a) XRD pattern of the prepared $Ba_{0.98}Sr_{0.02}Sn_{0.95}Mn_{0.05}O_3$ sample (JCPDS: 015-0780) and (b) the W–H plot of $Ba_{0.98}Sr_{0.02}Sn_{0.95}Mn_{0.05}O_3$.

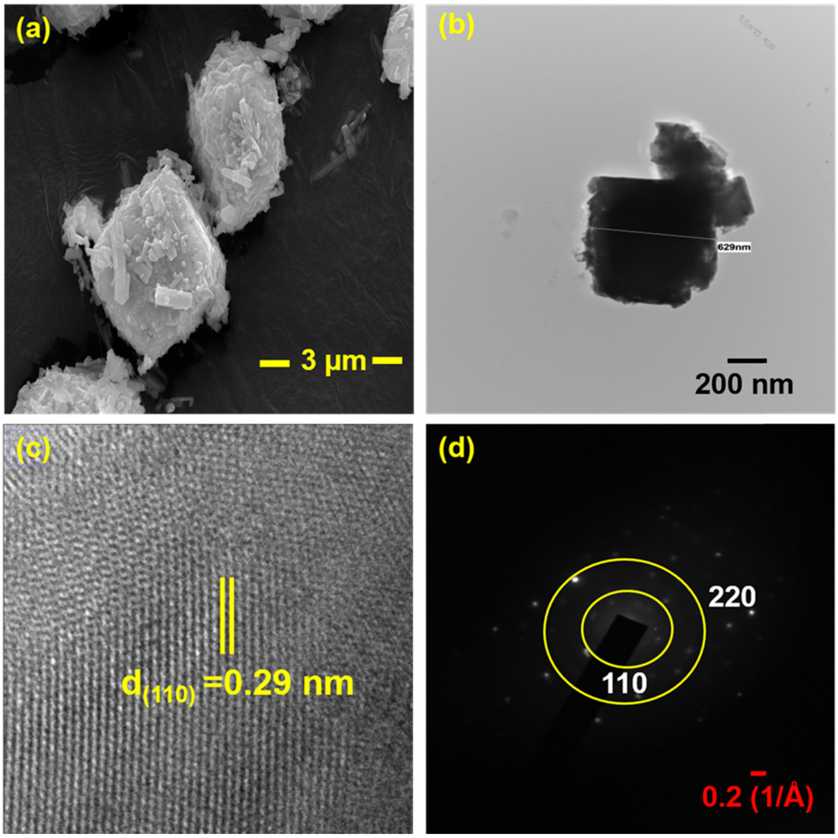

Fig. 2 (a) FESEM image, (b) TEM image, (c) HRTEM image, and (d) SAED image of $Ba_{0.98}Sr_{0.02}Sn_{0.95}Mn_{0.05}O_3$.

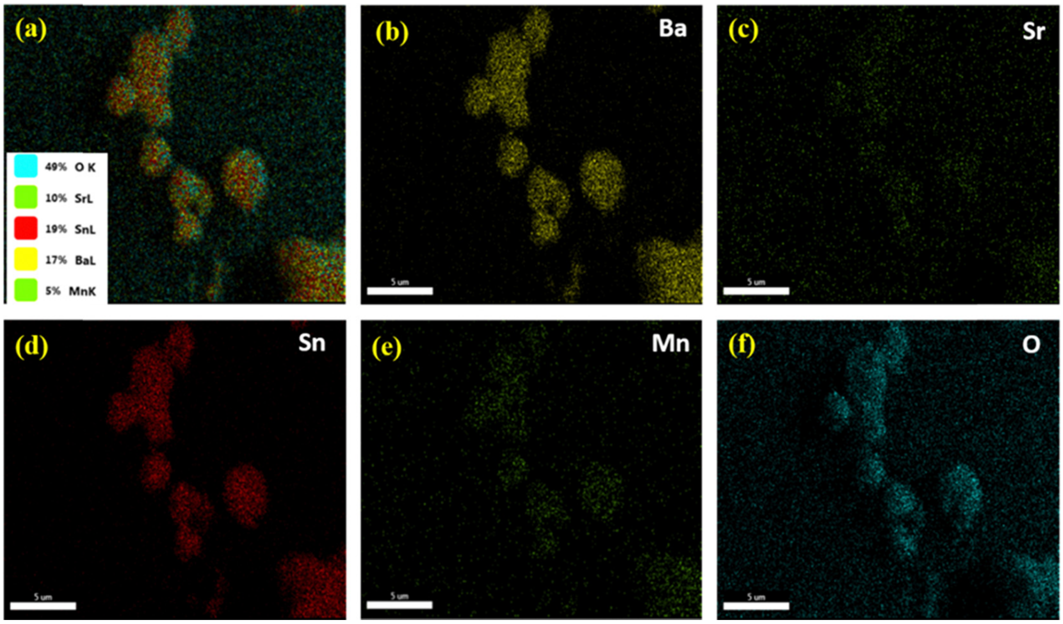

Fig. 3 (a) Elemental mapping and compositional analysis of $Ba_{0.98}Sr_{0.02}Sn_{0.95}Mn_{0.05}O_3$, (b) Ba (17%), (c) Sr (10%), (d) Sn (19%), (e) Mn (5%), and (f) O (49%).

diffraction spots in the SAED patterns support this conclusion. Furthermore, most of the spots are on the concentric circular rings, indicating that the synthesized $Ba_{0.98}Sr_{0.02}Sn_{0.95}Mn_{0.05}O_3$ sample is polycrystalline.

3.3 BET analysis

The $Ba_{0.98}Sr_{0.02}Sn_{0.95}Mn_{0.05}O_3$ perovskite's specific surface area and pore size distribution were determined by using the density functional theory (density in this context refers to the statistical

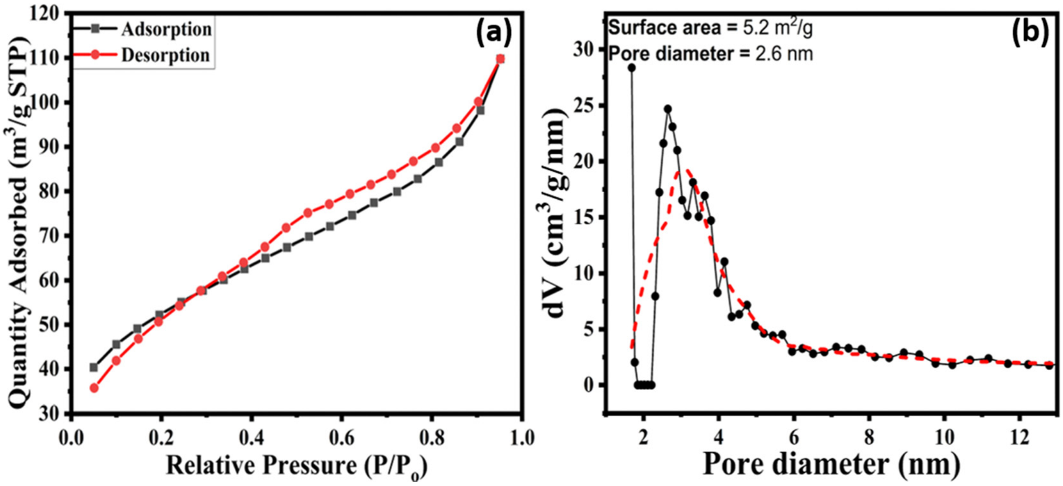

Fig. 4 (a) Nitrogen adsorption–desorption isotherms and (b) BJH pore-size distributions of $Ba_{0.98}Sr_{0.02}Sn_{0.95}Mn_{0.05}O_3$.

distribution of pores) to examine the desorption branch of N_2 gas isotherms. Nitrogen adsorption–desorption isotherms of $Ba_{0.98}Sr_{0.02}Sn_{0.95}Mn_{0.05}O_3$ show that it is a type IV isotherm (Fig. 4a), characteristic of a mesoporous material with a hysteresis loop at high partial pressures. As per the IUPAC classification of the hysteresis loop, the given isotherm for $Ba_{0.98}Sr_{0.02}Sn_{0.95}Mn_{0.05}O_3$ in Fig. 4a shows an H4-type hysteresis loop[61] with a narrow-slit pore (3.2 nm). It is observed that calcining the material at a low temperature and period of 700 °C and 2 h, respectively, promotes the formation of uniform narrow slit mesopores, which contributes to the sensing application by enhancing the sensor response of the material.[62,63] The BJH pore-size distributions (Fig. 4b) reveal the pore size to be 2.6 nm. The micrometer-cubic morphology formed from the plate-like hydroxylated cationic sheets under this calcination temperature and the relatively short time scale selected for our study would have stabilized narrow and mesoporous pores.

The flat band potential (E_{fb}) was calculated from the Mott–Schottky plot (Fig. 7d). The graph was plotted against $1/C^2$ *vs.* potential (V) and the line of intersection on the x-axis (potential) gave the value of E_{fb}, which is ~ -0.62 V. The negative value of the E_{fb} indicates downward band bending, which makes the flow of electrons easier[64,65] in the $Ba_{0.98}Sr_{0.02}Sn_{0.95}Mn_{0.05}O_3$ semiconductor perovskite.

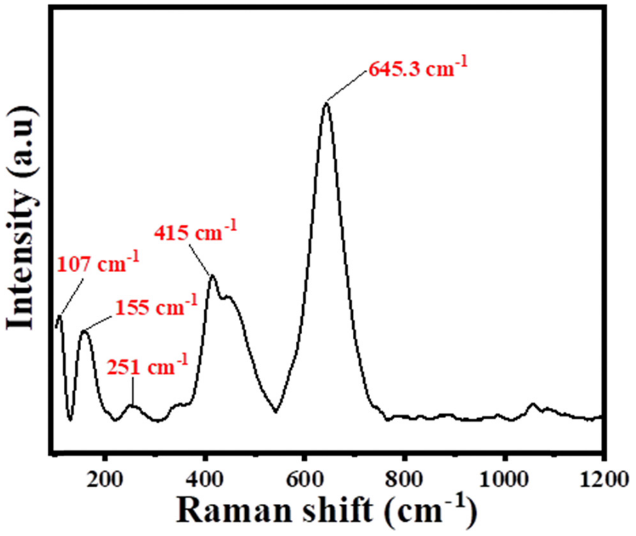

Fig. 5 The Raman spectra of the $Ba_{0.98}Sr_{0.02}Sn_{0.95}Mn_{0.05}O_3$ perovskite.

3.4 Raman analysis

Since BSO belongs to the space group $Pm\bar{3}m$, the $[SnO_6]$ octahedra may not show first-order Raman vibrational modes due to the centre of symmetry,[66,67] but there will always be some defect-induced vibrational modes as discussed subsequently.[68] However, since the dopants are introduced (Sr and Mn), there's a slight distortion in the $[SnO_6]$ octahedra, which facilitates the Raman vibration. The presence of oxygen vacancies and defect-oriented development might cause the observed Raman activity. In Fig. 5, the Raman peaks at 109 cm^{-1}, 155 cm^{-1}, 251 cm^{-1}, and 415 cm^{-1} are attributed to $[SnO_6]$ vibrational modes. The peak observed at 645 cm^{-1} is due to the SnO_6 vibrational mode, which becomes broad because of the presence of $[MnO_6]$ stretching modes[42] after Mn doping (Fig. S8, ESI†). Since vibrational Raman modes of MnO_2 are less dominant in our sample,[69,70] only stretching vibrations of $[MnO_6]$ have been shown to reside between 500 and 700 cm^{-1}.[71] It is to be noted that the size of Mn^{4+} is smaller than that of the Sn^{4+} ion and hence it can substitute the Sn^{4+} ion. The Raman peak of $[MnO_6]$ at 643 cm^{-1} coincides with the broad peaks attributed to $[SnO_6]$ (640 cm^{-1}). The Raman peaks of both Mn-doped and undoped $Ba_{0.98}Sr_{0.02}SnO_3$ substrates and their details are mentioned in the ESI.† It was observed that the carbonate peak at 1054 cm^{-1} diminishes with the increase in the concentration of Mn (Fig. S8, ESI†). A possible reason for this observation is that the interstitial carbon is replaced by the Mn^{4+} ion to form a trace amount of MnO_2 (not detected in the XRD of our sample) close to the surface of the nanocrystalline grains, with the increase in the concentration of Mn in (Ba, Sr)(Sn, Mn)O_3.

3.5 UV-visible analysis

Doping the right quantity of Mn adjusts the bandgap of BSO, an ultraviolet-absorbing material useful for visible light harvesting applications. The bandgap in $Ba_{0.98}Sr_{0.02}Sn_{1-x}Mn_xO_3$ reduces when the Mn concentration increases.[72] Tauc's plot (Fig. S7d ESI†) shows an indirect bandgap of 0.41 eV for $Ba_{0.98}Sr_{0.02}Sn_{0.95}Mn_{0.05}O_3$. The reduction in bandgap with the increase in the concentration of Mn may be possibly due to the presence of defects and hydroxylated cations. All these effects synergistically contribute towards the reduction of the energy level. The Tauc plot for the Mn-doped and undoped $Ba_{0.98}Sr_{0.02}SnO_3$ is presented in the ESI† (Fig. S7).

3.6 XPS analysis

The presence of elements and their oxidation states were determined by XPS analysis. Fig. 6 shows the XPS peaks for $Ba_{0.98}Sr_{0.02}Sn_{0.95}Mn_{0.05}O_3$. From the XPS spectra (Fig. 6a), the presence of constituent elements Ba, Sr, Sn, Mn, and O was identified in the synthesised $Ba_{0.98}Sr_{0.02}Sn_{0.95}Mn_{0.05}O_3$ perovskite. Fig. 6b gives a core level binding energy of Ba and there are doublet peaks that appear at 780.03 eV and 795.40 eV assigned to Ba $3d_{5/2}$ and Ba $3d_{3/2}$ respectively. The difference in these two peaks is 15.37 eV, which matches the reported data and confirms Ba's existence in the Ba^{2+} oxidation state.[73] Fig. 6c shows core-level splitting of Sr. In this, there are shoulder peaks that appear at 135.22 eV and 138.22 eV, assigned to Sr $3d_{5/2}$ and Sr $3d_{3/2}$ respectively. The difference in these two peaks is 2.97 eV which confirms the existence of Sr in the Sr^{2+} oxidation state as per the reported data.[74] The core-level binding energy of Sn is given in Fig. 6d. There are doublet peaks that appear at 486.28 eV and 494.71 eV which are assigned to Sn $3d_{5/2}$ and Sn $3d_{3/2}$ respectively. The difference in these two peaks is 8.43 eV which confirms the existence of Sn in the Sn^{4+} oxidation state as per the data.[75] A core-level binding energy of Mn can be seen in Fig. 6e. In this, there doublet peaks that appear at 641.74 eV and 652.96 eV which are assigned to Mn $2p_{3/2}$ and Mn $2p_{1/2}$ respectively. The difference in these two peaks is 11.22 eV, which confirms the existence of Mn in the Mn^{+4} oxidation state as per the reported data.[76,77] A single peak incorporating other small peaks for O 1s is observed in Fig. 6f. There are two peaks at 529.22 eV and 531.38 eV which are assigned to lattice oxygen and oxygen (O^{2-}) in the oxygen vacant region (oxygen vacancy) respectively.[78,79]

3.7 Sensing analysis

The sensing experiment was carried out for $Ba_{0.98}Sr_{0.02}Sn_{0.95}Mn_{0.05}O_3$ deposited over the trench of the ITO plate under ambient conditions (~25 °C) and was probed for ethanol gas. The sensor response for different Mn-doped $Ba_{0.98}Sr_{0.02}Sn_{0.95}Mn_{0.05}O_3$ was also studied along with $Ba_{0.98}Sr_{0.02}Sn_{0.95}Mn_{0.05}O_3$, but it showed no good sensor response. The sensor response for the $Ba_{0.98}Sr_{0.02}Sn_{0.95}Mn_{0.05}O_3$ substrate for different concentrations of ethanol was also studied, and it was found that 100 ppm of ethanol shows the best results as compared to 25 ppm and 50 ppm of ethanol (Fig. 7a). Unlike other Mn-doped $Ba_{0.98}Sr_{0.02}SnO_3$ substrates, $Ba_{0.98}Sr_{0.02}Sn_{0.95}Mn_{0.05}O_3$ shows a good sensitivity at room temperature (~25 °C) for ethanol, IPA, and acetone, *i.e.*, above 85%. It is observed that the sensitivity almost remains stable and is above 85%. The sensor response of all three VOCs is shown in Fig. 7e. A comparative graph giving insights into the response and recovery time of these three VOCs is demonstrated in Fig. 7f. The uniform cycles obtained for the $Ba_{0.98}Sr_{0.02}Sn_{0.95}Mn_{0.05}O_3$ sensor substrate (Fig. 7b) show a prompt response and recovery time for ethanol (100 ppm) at

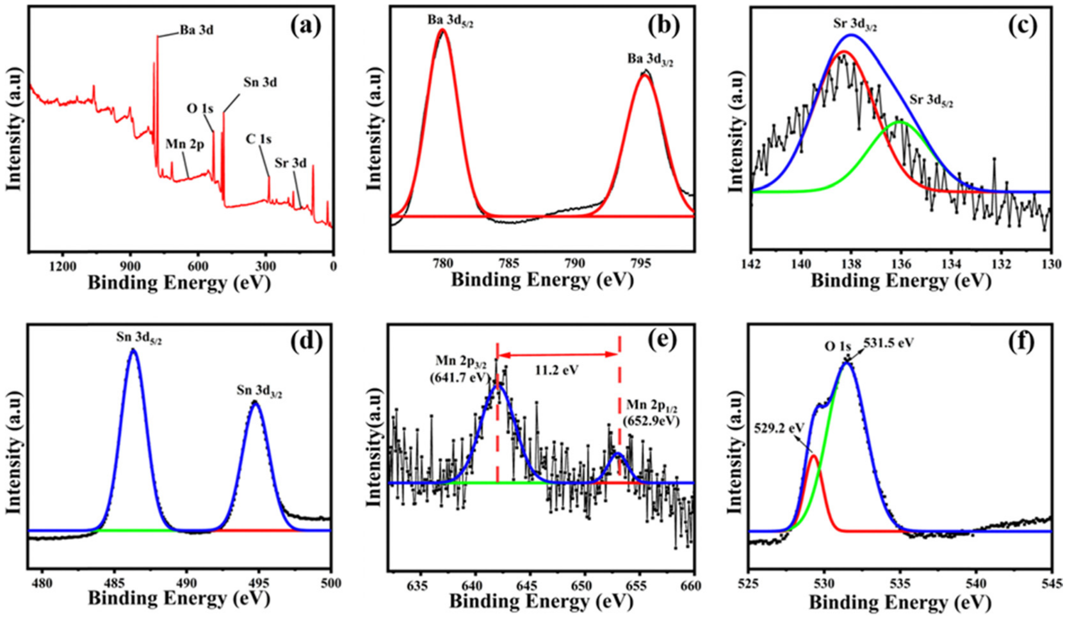

Fig. 6 XPS analysis of $Ba_{0.98}Sr_{0.02}Sn_{0.95}Mn_{0.05}O_3$: (a) XPS survey spectrum, (b) core level binding energy peaks of Ba, (c) core energy binding energy peaks of Sr, (d) core energy binding energy peaks of Sn, (e) core energy binding energy peaks of Mn, and (f) core energy binding energy of O.

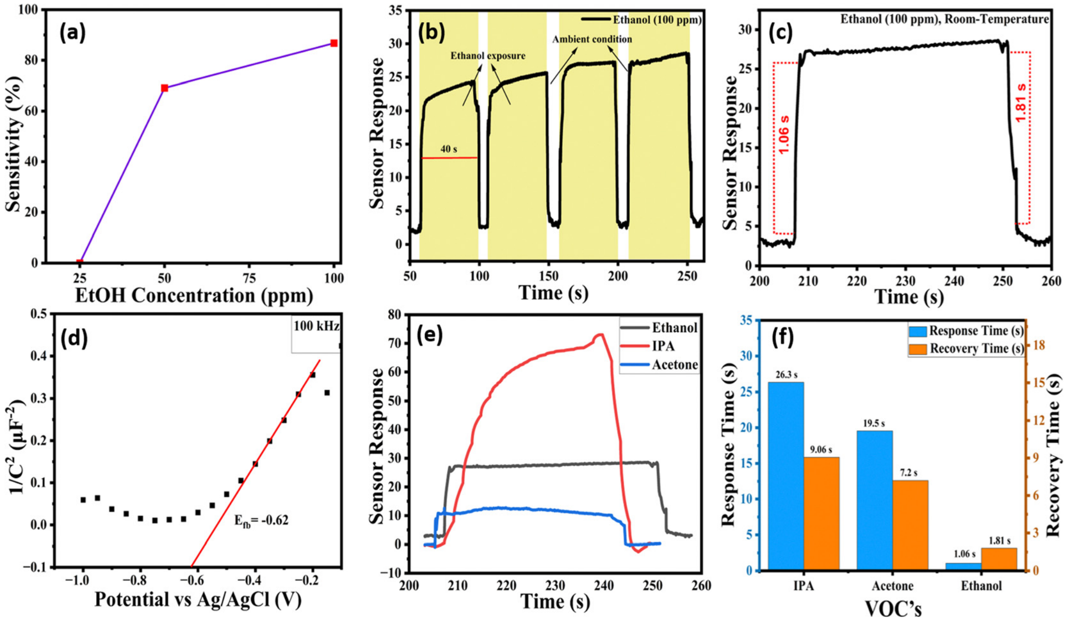

Fig. 7 (a) A plot of sensitivity *vs.* concentration of EtOH (ppm) for $Ba_{0.98}Sr_{0.02}Sn_{0.95}Mn_{0.05}O_3$, (b) a plot of sensor response *vs.* time for 100 ppm EtOH at room temperature (∼25 °C) and a humidity of 55% for $Ba_{0.98}Sr_{0.02}Sn_{0.95}Mn_{0.05}O_3$, (c) response and recovery times for 100 ppm ethanol of the $Ba_{0.98}Sr_{0.02}Sn_{0.95}Mn_{0.05}O_3$ substrate probed at room temperature (∼25 °C) and a humidity of 55%, (d) Mott–Schottky plot for $Ba_{0.98}Sr_{0.02}Sn_{0.95}Mn_{0.05}O_3$ showing a positive slope (n-type), (e) a plot of sensor response *vs.* time for different VOCs, and (f) comparative bar graphs of response and recovery times for different VOCs (100 ppm) at room temperature (∼25 °C).

1.06 s and 1.81 s, respectively (Fig. 7c), compared to the other VOCs (100 ppm), which shows its selectivity for ethanol, as the dipole moment and electron affinities are unique for every gas species. The above response was recorded at room temperature (∼25 °C) and a humidity of ∼55% during summer. This is one of the best results compared to the one recorded to date and is tabulated in Table S1 (ESI†) based on the response and recovery time. However, the stability of the same substrate when probed after 5 months (during the rainy season) showed a sensitivity of 88% with a humidity of about 85%. Due to high humidity, there was a delay in the response and recovery time. The response and recovery time were recorded as 16 s and 4 s, respectively (Fig. S10a and b, ESI†). At low humidity, fewer water molecules interact with the $Ba_{0.98}Sr_{0.02}Sn_{0.95}Mn_{0.05}O_3$ sensor substrate thereby reducing the dissociation of water. It is known that the hydroxyl group impedes the adsorption of oxygen species.[80,81] The repeatability of the sensor substrate was also probed for 1100 s, and it showed sensitivity above 85% (Fig. 8a) with response and recovery times of 20.3 s and 4.2 s, respectively at ∼70% humidity for ethanol (100 ppm). The decrease in the intensity of the peaks with an increase in time (s) is due to the decrease in the concentration of ethanol gas which occurs while placing the sensor substrate in

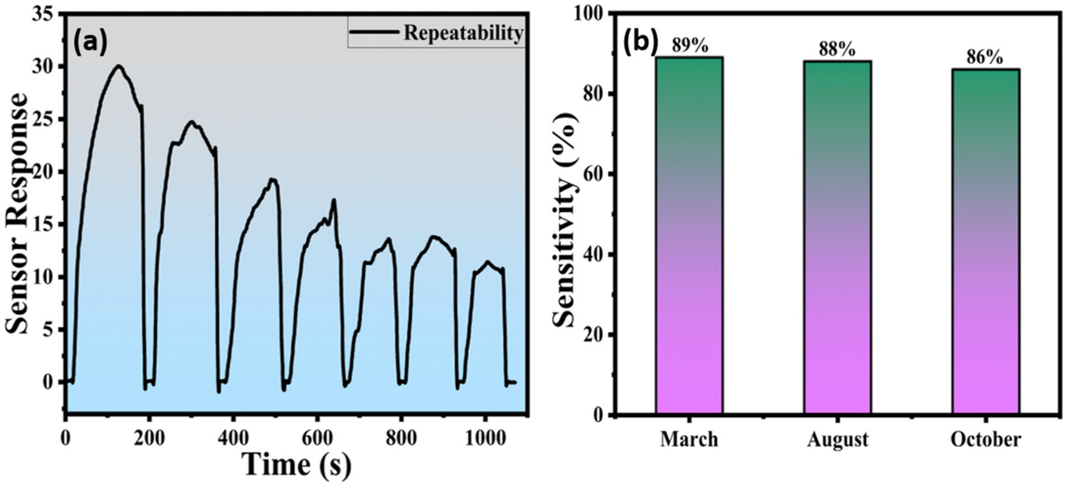

Fig. 8 (a) Repeatability of the sensor substrate $Ba_{0.98}Sr_{0.02}Sn_{0.95}Mn_{0.05}O_3$ at room temperature (∼25 °C) and a humidity of ∼70% for ethanol (100 ppm) and (b) the sensitivity of the $Ba_{0.98}Sr_{0.02}Sn_{0.95}Mn_{0.05}O_3$ sensor substrate probed in March, August and October (2024).

(ethanol exposure) and taking it off (ambient condition) the gas chamber, which is done manually. Fig. 8b shows the stability of the sensor substrate based on sensitivity recorded for different months, *i.e.*, in March, August, and October the sensitivity (humidity) was 89% (∼55%), 88% (∼85%), and 86% (∼70%), respectively. There is not much change in the sensitivity even after seven months. The sensitivity was above 85% for the recorded months.

The electron densities in BSO can be increased by introducing a donor dopant,[82,83] by oxide reduction (which occurs due to the presence of oxygen vacancies and creating electrons),[1,84,85] and by charge transfer that takes place at the interface.[86] EDS and XPS data of $Ba_{0.98}Sr_{0.02}Sn_{0.95}Mn_{0.05}O_3$ reveal the presence of oxygen vacancies which act as electron donors and result in n-type carriers. The number of donors (N_d) present in $Ba_{0.98}Sr_{0.02}Sn_{0.95}Mn_{0.05}O_3$ is of the order of 10^{24} cm^{-3}.[1,87] These electrons interact with the atmospheric oxygen molecules and form oxygen species, further interacting with the ethanol molecules, thereby giving a prompt sensor response.

At high humidity, H_2O molecules compete with the charge traps with O_2^- on the surface thereby restricting O_2 adsorption. H_2O molecules may further develop a hydrogen-bonded network to capture more O_2 or H_2O by even eliminating O_2^-.[88] The supercell models of the perovskite solid solution having ethanol or water molecules show that the molecules would orient along the edges of the [Sn/Mn] centred polyhedral network in the presence of defects like oxygen vacancies or adsorbed oxygen. These favourable orientations would facilitate ethanol oxidation (Fig. S12a and b, ESI†). Santiburcio and Marx[89] have studied the structural and dynamic properties of nano-confined water and hydroxylated species in FeS sheets having mesoporous slit pores. They concluded that the polar species prefer to perpendicularly orient along the surfaces of the slit pores. Humidity-dependent pore closing/opening within narrow slit pores have been theoretically modelled by Schiller *et al.*[90] In a relatively low-humid environment, the sensitivity of the EtOH molecules is improved in our sample ($Ba_{0.98}Sr_{0.02}Sn_{0.95}Mn_{0.05}O_3$) due to the presence of low-hydroxylated pores.

The introduction of Mn into $Ba_{0.98}Sr_{0.02}Sn_0O_3$ gives rise to more oxygen vacancies, as seen from the intense peak of the XPS data for O 1s. It is also known that Mn ions in the perovskites have high affinity towards adsorbed oxygen species.[45] The evidence of oxygen vacancies is confirmed by the presence of the O 1s peak at 531 eV in the XPS spectra. These oxygen vacancies act like electron traps,[91] which later participate in the reaction when the sensor substrate is exposed to the volatile compounds. At higher temperatures, the lattice oxygen is released, giving rise to oxygen vacancies.[92] $Ba_{0.98}Sr_{0.02}Sn_{0.95}Mn_{0.05}O_3$ shows a good sensor response due to the presence of oxygen vacancies and the absence of the adsorbed OH groups that hinder the interaction between the substrate and the target gas. It also has a high surface area of 5.208 m^2 g^{-1}, which provides enough space for the interaction. A positive Mott–Schottky slope indicates that $Ba_{0.98}Sr_{0.02}Sn_{0.95}Mn_{0.05}O_3$ is an n-type semiconductor (Fig. 7d). The interaction of the gaseous species with the n-type semiconductor ($Ba_{0.98}Sr_{0.02}Sn_{0.95}Mn_{0.05}O_3$) involves two major steps. The first interaction of the semiconductor occurs with the atmospheric oxygen molecule. Oxygen molecules being highly electronegative easily get adsorbed over the sensor's surface. This adsorbed oxygen molecule withdraws electrons from the sensor's conduction band. It forms a chemisorbed oxygen species like O_2^-, O^-, and O^{2-} as shown in the equation below. These adsorbed oxygen species exhibit superior ethanol adsorption across the surface because of their great affinity for the polar O–H bond of ethanol.[93] Moreover, as proposed by Singh *et al.*[19] in their ethanol sensing mechanism, the dominant species adsorbed at room temperature is likely to be O_2^-. Adsorbed oxygen species in the presence of oxygen vacancies facilitate the oxidation process.

$$O_2 + e^- \rightarrow O_2^-{}_{(ads)} \tag{3}$$

$$O_2^-{}_{(ads)} + e^- \rightarrow O^-{}_{(ads)} \tag{4}$$

$$O^-{}_{(ads)} + e^- \rightarrow O^{2-}{}_{(ads)} \tag{5}$$

After further reaction with the adsorbed oxygen species, these adsorbed oxygen species react with ethanol and oxidise it to produce CO_2, H_2O and free electrons.

$$C_2H_5OH + 6O^-{}_{(ads)} \rightarrow 2CO_2 + 3H_2O + 6e^- \tag{6}$$

$$C_2H_5OH + 6O^{2-}{}_{(ads)} \rightarrow 2CO_2 + 3H_2O + 12e^- \tag{7}$$

The narrow-slit pores present in $Ba_{0.98}Sr_{0.02}Sn_{0.95}Mn_{0.05}O_3$ enhance the oxidation process of EtOH at 55% humidity. Fig. 9 shows the layer of H_2O over the surface of the particles that hinders the oxidation of EtOH at 85% humidity, resulting in a delay in the response and recovery time as mentioned earlier.

4. Conclusion

In this study, $Ba_{0.98}Sr_{0.02}Sn_{0.95}Mn_{0.05}O_3$ was prepared using a chemical co-precipitation method at a low temperature of 700 °C. The XRD peaks reveal the formation of the cubic phase of the $Ba_{0.98}Sr_{0.02}Sn_{0.95}Mn_{0.05}O_3$ perovskite, the crystallite size was determined to be 28 nm and the positive slope of the W–H plot shows that the perovskite undergoes a microstrain of the order 10^{-3}. The FESEM and TEM images show the formation of cube-like structures. The surface area of $Ba_{0.98}Sr_{0.02}Sn_{0.95}Mn_{0.05}O_3$ was high compared to that of the other Mn-doped/undoped $Ba_{0.98}Sr_{0.02}SnO_3$, enhancing the sensor activity. The Raman analysis shows the vibrational modes for octahedral [SnO_6] and MnO_2, which are formed over the surface of the cube. Unlike the XRD pattern, the Raman spectra reveal the formation of MnO_2. Optical studies determine $Ba_{0.98}Sr_{0.02}Sn_{0.95}Mn_{0.05}O_3$ to be near-infrared active having an indirect bandgap of 0.41 eV. The surface area of $Ba_{0.98}Sr_{0.02}Sn_{0.95}Mn_{0.05}O_3$ was calculated to be 5.208 m^2 g^{-1}. The response and recovery times for different Mn-doped substrates were analysed, and the $Ba_{0.98}Sr_{0.02}Sn_{0.95}Mn_{0.05}O_3$ substrate showed the shortest response and recovery time of 1.06 s and 1.81 s (55% humidity), respectively, which is one of the best time-scales recorded to date for ethanol sensing at room temperature (∼25 °C). The substrate shows sensitivity above 85% even after 7 months. However, there is a further scope for advanced measurements and computational studies. For example, it will be

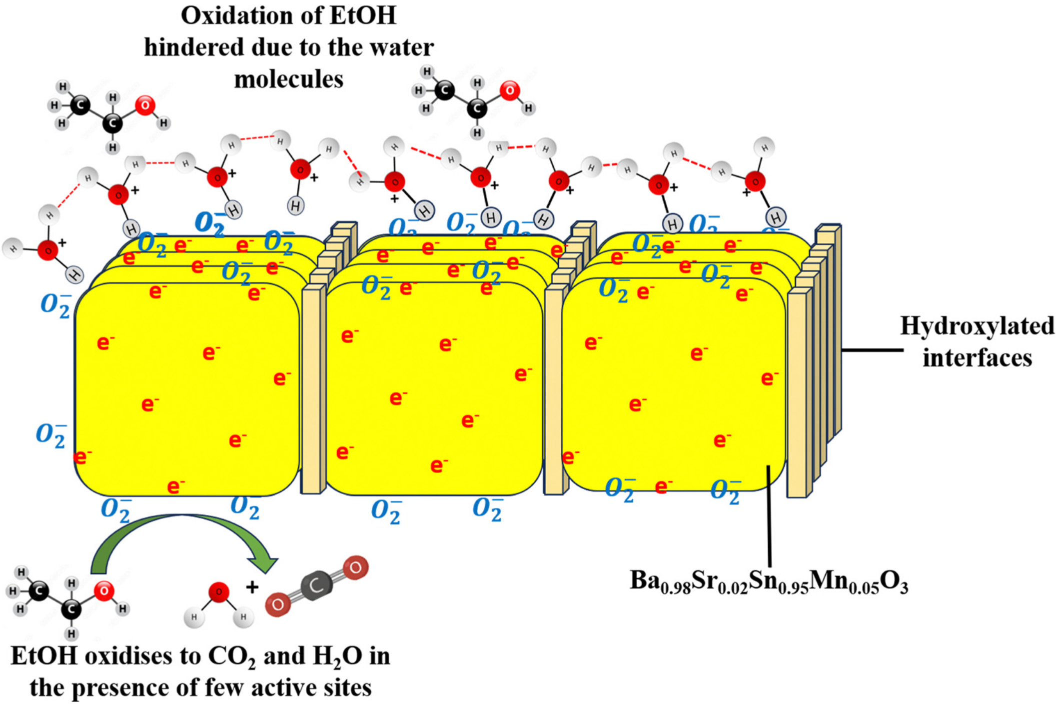

Fig. 9 Oxidation of EtOH over the surface of the $Ba_{0.98}Sr_{0.02}Sn_{0.95}Mn_{0.05}O_3$ perovskite hindered due to the formation of an H_2O layer over the surface of the particles at 85% humidity.

worthwhile to carry out humidity-controlled sensing measurements so that detection limits and sensing stability can be thoroughly investigated. In addition to detailed experimental analysis, higher-level computational methods such as simulation of the dynamic adsorption–desorption process would help delineate the ethanol–stannate perovskite solid solution interaction. Though replicating the exact composition of solid-solution for modelling is difficult, computational modelling provides valuable insights into the nature of adsorption at the molecule-solid surface.

Author contributions

NAW: conceptualization, investigation, validation and manuscript writing. KPJ: supervision, methodology, resources, validation and manuscript review.

Data availability

The supporting document has been provided which comprises all data that supports the research work.

Conflicts of interest

There are no conflicts to declare.

Acknowledgements

The authors gratefully acknowledge Prof. Teny Theresa John and Ms Vaishnavi Mohan from Semiconductors Materials and Device Laboratory, Department of Physics, BITS Pilani, KK Birla Goa campus for assisting in the Sensor experiments and helpful discussions. The authors would like to thank Prof. Halan Prakash and Prof. Kiran Vankayala for their helpful discussion of structural analysis during the project. The authors are thankful to Mr Laxman G. Raikar for assisting in the EIS analysis. The authors are also thankful to CSIF Laboratory, BITS Pilani, KK Birla Goa Campus, CAL BITS Pilani Hyderabad Campus (XPS analysis), SPPU (TGA/DSC analysis), Shivaji University (TEM and SAED analysis), Department of Chemistry, BITS Pilani, KK Birla Goa Campus for giving access to BET, EIS, UV-visible spectroscopy analysis, and DST-SERB for the computational facility (desktop server for small scale computations) through a recently completed project. Nehal Waghchoure gratefully acknowledges BITS Pilani, KK Birla Goa Campus for providing the PhD fellowship. The authors gratefully acknowledge BITS Pilani KK Birla Goa Campus for providing financial support for the PhD Research Project.

References

1 W.-J. Lee, H. J. Kim, J. Kang, D. H. Jang, T. H. Kim, J. H. Lee and K. H. Kim, *Annu. Rev. Mater. Res.*, 2017, **47**, 391–423.
2 H. Mizoguchi, P. Chen, P. Boolchand, V. Ksenofontov, C. Felser, P. W. Barnes and P. M. Woodward, *Chem. Mater.*, 2013, **25**, 3858–3866.
3 K. Li, Q. Gao, L. Zhao, K. Lv, L. Yin and Q. Liu, *Appl. Phys. Lett.*, 2020, **117**, 072101.
4 J. John, S. R. Chalana, R. Prabhu and V. P. Mahadevan Pillai, *Appl. Phys. A: Mater. Sci. Process.*, 2019, **125**, 155.

5 Y. H. Ochoa-Muñoz, J. E. Rodríguez-Páez and R. Mejía de Gutiérrez, *Mater. Chem. Phys.*, 2021, **266**, 124557.

6 F. Zhong, H. Zhuang, Q. Gu and J. Long, *RSC Adv.*, 2016, **6**, 42474–42481.

7 I. Kocemba, J. Długołęcka, M. Wróbel-Jędrzejewska, J. Rogowski, I. Dobrosz-Gómez and J. Rynkowski, *React. Kinet., Mech. Catal.*, 2018, **123**, 659–677.

8 A. Roy, P. P. Das, P. Selvaraj, S. Sundaram and P. S. Devi, *ACS Sustainable Chem. Eng.*, 2018, **6**, 3299–3310.

9 A. Soultati, M. Tountas, K. K. Armadorou, Abd R. Bin M. Yusoff, M. Vasilopoulou and M. K. Nazeeruddin, *Energy Adv.*, 2023, **2**, 1075–1115.

10 S. S. Shin, J. S. Kim, J. H. Suk, K. D. Lee, D. W. Kim, J. H. Park, I. S. Cho, K. S. Hong and J. Y. Kim, *ACS Nano*, 2013, **7**, 1027–1035.

11 S. N. Khan, A. Jehan, M. Husain, N. Rahman, V. Tirth, S. A. Shah, M. Uzair, M. Y. Khan, N. Sfina, M. Elhadi, A. Alotaibi and A. Khan, *Optik*, 2024, **303**, 171724.

12 H. Taz, B. Prasad, Y. L. Huang, Z. Chen, S. L. Hsu, R. Xu, V. Thakare, T. S. Sakthivel, C. Liu, M. Hettick, R. Mukherjee, S. Seal, L. W. Martin, A. Javey, G. Duscher, R. Ramesh and R. Kalyanaraman, *Sci. Rep.*, 2020, **10**, 3583.

13 S. A. Mir, A. Q. Seh and D. C. Gupta, *RSC Adv.*, 2020, **10**, 36241–36252.

14 S. Tao, F. Gao, X. Liu and O. T. Sùrensen, *Sens. Actuators, B*, 2000, **71**, 223–227.

15 J. Yu, R. Ran, Y. Zhong, W. Zhou, M. Ni and Z. Shao, *Energy Environ. Mater.*, 2020, **3**, 121–145.

16 H. Li, X. Shi, X. Liu and X. Li, *Appl. Surf. Sci.*, 2020, **508**, 145306.

17 Y. Liu, W. Wang, X. Xu, J.-P. Marcel Veder and Z. Shao, *J. Mater. Chem., A*, 2019, **7**, 7280.

18 J. M. Rondinelli, S. J. May and J. W. Freeland, *MRS Bull.*, 2012, **37**, 261–270.

19 P. Singh, N. K. Bansal, S. Dey, R. Singh and T. Singh, *Langmuir*, 2024, **40**, 21931–21956.

20 T. H. Bui and J. H. Shin, *Microchem. J.*, 2023, **191**, 108924.

21 J. Park, Y. N. Wu, W. A. Saidi, B. Chorpening and Y. Duan, *Chem. Phys. Chem.*, 2020, **22**, 27163–27172.

22 Z. Li, H. Li, Z. Wu, M. Wang, J. Luo, H. Torun, P. Hu, C. Yang, M. Grundmann, X. Liu and Y. Fu, *Mater. Horiz.*, 2019, **6**, 470.

23 C. He, J. Cheng, X. Zhang, M. Douthwaite, S. Pattisson and Z. Hao, *Chem. Rev.*, 2019, **119**, 4471–4568.

24 Y. Zhang, J. Zhang, Y. Jiang, Z. Duan, B. Liu, Q. Zhao, S. Wang, Z. Yuan and H. Tai, *Sens. Actuators, B*, 2020, **319**, 128293.

25 Z. L. Chen, D. Wang, X.-Y. Wang and J.-H. Yang, *Rare Met.*, 2021, **40**, 1561–1570.

26 S. Acharyya, S. Nag, S. Kimbahune, A. Ghose, A. Pal and P. K. Guha, *ACS Sens.*, 2021, **6**, 2218–2224.

27 Z. Li, X. Liu, M. Zhou, S. Zhang, S. Cao, G. Lei, C. Lou and J. Zhang, *J. Hazard. Mater.*, 2021, **415**, 125757.

28 D. L. Feng, Z. Y. Zhu, L. L. Du, X. X. Xing, C. Wang, J. Chen, Y. T. Tian and D. C. Yang, *Rare Met.*, 2021, **40**, 1642–1650.

29 A. A. Felix, R. A. Silva and M. O. Orlandi, *CrystEngComm*, 2020, **22**, 4640–4649.

30 X. Chang, X. Li, X. Qiao, K. Li, Y. Xiong, X. Li, T. Guo, L. Zhu and Q. Xue, *Sens. Actuators, B*, 2020, **304**, 127430.

31 Y. C. Wang, Z. Sen Sun, S. Z. Wang, S. Y. Wang, S. X. Cai, X. Y. Huang, K. Li, Z. T. Chi, S. Di Pan and W. F. Xie, *J. Mater. Sci.*, 2019, **54**, 14055–14063.

32 T. Zhang, X. Tang, J. Zhang, T. Zhou, H. Wang, C. Wu, X. Xia, C. Xie and D. Zeng, *Langmuir*, 2018, **34**, 14577–14585.

33 Y. Zhou, Q. Ding, J. Li, Y. Wang, B. Wang, W. Zhu, X. OuYang, L. Liu and Y. Wang, *J. Alloys Compd.*, 2019, **811**, 151958.

34 J. N. Mao, B. Hong, H. D. Chen, M. H. Gao, J. C. Xu, Y. B. Han, Y. T. Yang, H. X. Jin, D. F. Jin, X. L. Peng, J. Li, H. L. Ge and X. Q. Wang, *J. Alloys Compd.*, 2020, **827**, 154248.

35 Z. Da Hu, X. Y. Sun, H. F. Li, Y. R. Kang, X. Q. Song, P. Wang, Q. T. Luan, X. D. Wang, Z. T. Chi and W. F. Xie, *Rare Met.*, 2021, **40**, 1554–1560.

36 P. Tiwary, S. G. Chatterjee, S. S. Singha, R. Mahapatra and A. K. Chakraborty, *FlatChem.*, 2021, **30**, 100317.

37 C. W. Na, H. S. Woo, I. D. Kim and J. H. Lee, *Chem. Commun.*, 2011, **47**, 5148–5150.

38 M. Khatib and H. Haick, *ACS Nano*, 2022, **16**, 7080–7115.

39 N. Yamazoe, *Sens. Actuators, B*, 2005, **108**, 2–14.

40 S. Zhao, Y. Shen, F. Hao, C. Kang, B. Cui, D. Wei and F. Meng, *Appl. Surf. Sci.*, 2021, **538**, 148140.

41 G. Korotcenkov, *Mater. Sci. Eng., B*, 2007, **139**, 1–23.

42 K. Balamurugan, N. Harish Kumar, B. Ramachandran, M. S. Ramachandra Rao, J. Arout Chelvane and P. N. Santhosh, *Solid State Commun.*, 2009, **149**, 884–887.

43 C. Gan, Y. Zhang, D. Battaglia, X. Peng and M. Xiao, *Appl. Phys. Lett.*, 2008, **92**, 241111.

44 V. Pinchetti, A. Anand, Q. A. Akkerman, D. Sciacca, M. Lorenzon, F. Meinardi, M. Fanciulli, L. Manna and S. Brovelli, *ACS Energy Lett.*, 2019, **4**, 85–93.

45 M. A. Peña and J. L. G. Fierro, *Chem. Rev.*, 2001, **101**, 1981–2017.

46 S. Mahatara, S. Thapa, H. Paik, R. Comes and B. Kiefer, *ACS Appl. Mater. Interfaces*, 2022, **14**, 45025–45031.

47 T. Mohan, S. Kuppusamy and R. J. V. Michael, *ACS Omega*, 2022, **7**, 18531–18541.

48 C. Li, K. C. K. Soh and P. Wu, *J. Alloys Compd.*, 2004, **372**, 40–48.

49 C. Udawatte, *Solid State Ionics*, 2000, **128**, 217–226.

50 S. M. de Freitas, G. J. B. Júnior, R. D. S. Santos and M. V. dos S. Rezende, *Comput. Condens. Matter*, 2019, **21**, e00411.

51 M. H. Whangbo, E. E. Gordon, J. L. Bettis, A. Bussmann-Holder and J. Köhler, *Z. Anorg. Allg. Chem.*, 2015, **641**, 1043–1052.

52 J. John, M. Dhananjaya, S. Suresh, S. Savitha Pillai, M. Sahoo, O. M. Hussain, R. Philip and V. P. Mahadevan Pillai, *J. Mater. Sci.: Mater. Electron.*, 2020, **31**, 11159–11176.

53 J. Miao, X. Duan, J. Li, J. Dai, B. Liu, S. Wang, W. Zhou and Z. Shao, *J. Chem. Eng.*, 2019, **355**, 721–730.

54 S. Sun and S. Liang, *J. Mater. Chem. A*, 2017, **5**, 20534–20560.

55 E. P. Nascimento, H. C. T. Firmino, A. M. C. Santos, H. B. Sales, V. D. Silva, D. A. Macedo, G. A. Neves, E. S. Medeiros and R. R. Menezes, *J. Am. Ceram. Soc.*, 2021, **104**, 1297–1308.

56 Q. Chen, S. Y. Ma, X. L. Xu, H. Y. Jiao, G. H. Zhang, L. W. Liu, P. Y. Wang, D. J. Gengzang and H. H. Yao, *Sens. Actuators, B*, 2018, **264**, 263–278.

57 S. Kumar and T. T. John, *Appl. Surf. Sci.*, 2023, **620**, 156816.

58 R. D. Shannon, *Acta. Crystallogr., Sect. A*, 1976, **32**, 751–767.

59 A. S. Deepa, S. Vidya, P. C. Manu, S. Solomon, A. John and J. K. Thomas, *J. Alloys Compd.*, 2011, **509**, 1830–1835.

60 H. Mizoguchi, N. S. P. Bhuvanesh, Y. Il Kim, S. Ohara and P. M. Woodward, *Inorg. Chem.*, 2014, **53**, 10570–10577.

61 M. Thommes, K. Kaneko, A. V. Neimark, J. P. Olivier, F. Rodriguez-Reinoso, J. Rouquerol and K. S. W. Sing, *Pure Appl. Chem.*, 2015, **87**, 1051–1069.

62 L. Yuan, T. Hyodo, Y. Shimizu and M. Egashira, *Sensors*, 2011, **11**, 1261–1276.

63 Z. Y. Yuan, T. Z. Ren, A. Vantomme and B. L. Su, *Chem. Mater.*, 2004, **16**, 5096–5106.

64 A. Hankin, F. E. Bedoya-Lora, J. C. Alexander, A. Regoutz and G. H. Kelsall, *J. Mater. Chem. A*, 2019, **7**, 26162–26176.

65 M. Radecka, M. Rekas, A. Trenczek-Zajac and K. Zakrzewska, *J. Power Sources*, 2008, **181**, 46–55.

66 J. Cerdà, J. Arbiol, R. Diaz, G. Dezanneau and J. R. Morante, *Mater. Lett.*, 2002, **56**, 131–136.

67 K. K. James, P. S. Krishnaprasad, K. Hasna and M. K. Jayaraj, *J. Phys. Chem. Solids*, 2015, **76**, 64–69.

68 S. A. Salehizadeh, H. M. Chenari, M. Shabani, H. A. Ahangar, R. Zamiri, A. Rebelo, J. S. Kumar, M. P. F. Graça and J. M. F. Ferreira, *RSC Adv.*, 2018, **8**, 2100–2108.

69 M. E. Becerra, N. P. Arias, O. H. Giraldo, F. E. López-Suárez, M. J. Illán-Gómez and A. Bueno-López, *Catalysts*, 2012, **2**, 352–367.

70 B. R. Strohmeier and D. M. Hercules, *Phys. Chem.*, 1984, **88**, 4922–4929.

71 C. M. Julien, *Solid State Ionics*, 2006, **177**, 11–19.

72 J. John, M. Dhananjaya, S. Suresh, S. Savitha Pillai, M. Sahoo, O. M. Hussain and R. Philip, and V. P. Mahadevan Pillai, *J. Mater. Sci.: Mater. Electron.*, 2020, **31**, 11159–11176.

73 J. John, S. Suresh, S. R. Chalana and V. P. Mahadevan Pillai, *Appl. Phys. A: Mater. Sci. Process.*, 2019, **125**, 743.

74 T. Mohan, S. Kuppusamy and R. J. V. Michael, *ACS Omega*, 2022, **7**, 18531–18541.

75 M. Kwoka and M. Krzywiecki, *Beilstein J. Nanotechnol.*, 2017, **8**, 514–521.

76 A. Prakash, P. Xu, A. Faghaninia, S. Shukla, J. W. Ager, C. S. Lo and B. Jalan, *Nat. Commun.*, 2017, **8**, 15167.

77 H. J. Kim, U. Kim, H. M. Kim, T. H. Kim, H. S. Mun, B. G. Jeon, K. T. Hong, W. J. Lee, C. Ju, K. H. Kimy and K. Char, *Appl. Phys. Express*, 2012, **5**, 061102.

78 K. Ganguly, A. Prakash, B. Jalan and C. Leighton, *APL Mater.*, 2017, **5**, 056102.

79 H. M. I. Jaim, S. Lee, X. Zhang and I. Takeuchi, *Appl. Phys. Lett.*, 2017, **111**, 172102.

80 T. R. Paudel and E. Y. Tsymbal, *Phys. Rev. B*, 2017, **96**, 245423.

81 K. Gelderman, L. Lee and S. W. Donne, *J. Chem. Educ.*, 2007, **84**(4), 685.

82 O. A. Bulavchenko, Z. S. Vinokurov, T. N. Afonasenko, P. G. Tsyrul'nikov, S. V. Tsybulya, A. A. Saraev and V. V. Kaichev, *Dalton Trans.*, 2015, **44**, 15499–15507.

83 H. W. Nesbitt and D. Banerjee, *Am. Mineral.*, 1998, **83**, 305–315.

84 L. Q. Wu, Y. C. Li, S. Q. Li, Z. Z. Li, G. D. Tang, W. H. Qi, L. C. Xue, X. S. Ge and L. L. Ding, *AIP Adv.*, 2015, **5**, 097210.

85 J. C. Dupin, D. Gonbeau, P. Vinatier and A. Levasseur, *Phys. Chem. Chem. Phys.*, 2000, **2**, 1319–1324.

86 D. Koziej, N. Bârsan, U. Weimar, J. Szuber, K. Shimanoe and N. Yamazoe, *Chem. Phys. Lett.*, 2005, **410**, 321–323.

87 A. Nasriddinov, M. Rumyantseva, E. Konstantinova, A. Marikutsa, S. Tokarev, P. Yaltseva, O. Fedorova and A. Gaskov, *Nanomaterials*, 2020, **10**(5), 915.

88 Y. H. Huang, T. Y. Yen, M. T. Shi, Y. H. Hung, W. T. Chen, C. H. Wu, K. M. Hung and K. Y. Lo, *Sens. Actuators, B*, 2023, **376**, 133011.

89 D. Muñoz-Santiburcio and D. Marx, *Nat. Commun.*, 2016, **7**, 12625.

90 P. Schiller, M. Wahab, T. A. Bier and H. J. Mögel, *Colloids Interfaces*, 2018, **2**(4), 62.

91 A. Shyichuk and E. Zych, *J. Phys. Chem. C*, 2020, **124**, 14945–14962.

92 J. Wang, D. N. Mueller and E. J. Crumlin, *J. Eur. Ceram. Soc.*, 2024, **44**, 116709.

93 Q. Fu, K. Lu, N. Li and Z. Dong, *Mater. Res. Bull.*, 2023, **168**, 112457.